Eleventh International Conference on Computational Fluid Dynamics (ICCFD11), Maui, Hawaii, July 11-15, 2022

ICCFD11-2022-0305

Anisotropic Mesh Modifications for the Moving Discontinuous Galerkin Method with Interface Condition Enforcement for Robust Simulations of High-Speed Viscous Flows

Eric J. Ching*, Andrew Kercher* and Andrew Corrigan*
Corresponding author: eric.ching@nrl.navy.mil

* Laboratories for Computational Physics and Fluid Dynamics,
U.S. Naval Research Laboratory, 4555 Overlook Ave SW, Washington, DC 20375.

Abstract: The moving discontinuous Galerkin method with interface condition enforcement (MDG-ICE) is a high-order, r-adaptive method that treats the grid as a variable and weakly enforces the conservation law, constitutive law, and corresponding interface conditions in order to implicitly fit high-gradient flow features. In this paper, we introduce anisotropic grid modifications to more robustly and efficiently compute high-speed viscous flows. Specifically, we incorporate an anisotropic grid regularization based on the mesh-implied metric into the nonlinear least-squares solver that inhibits grid motion in directions with small element length scales. Furthermore, we develop a dynamic grid refinement strategy that adds grid resolution only where necessary. We apply the proposed MDG-ICE formulation to test cases involving viscous shocks and/or boundary layers, including Mach 17.6 hypersonic viscous flow over a circular half-cylinder, a challenging test case for conventional numerical schemes on simplicial grids. The computed solutions are free from spurious oscillations and asymmetries. This work represents an intermediate step towards producing high-quality, anisotropic, feature-aligned grids with MDG-ICE. In future work, we will make further use of the provided metric, which intrinsically contains the necessary length scales as a result of the MDG-ICE formulation, and leverage metric-based mesh generation/adaptation.

Keywords: MDG-ICE, Shock fitting, Shock tracking, discontinuous Galerkin, high-order, r-adaptivity

1 Introduction

The moving discontinuous Galerkin finite element method with interface condition enforcement (MDG-ICE) is an implicit shock fitting method capable of handling complex shock dynamics [1, 2, 3]. The method is a unique variation of the well-known discontinuous Galerkin (DG) method. Specifically, neighboring elements are not coupled through interfacial, single-valued, numerical fluxes; instead, the conservation law and interface (Rankine-Hugoniot) conditions are directly discretized and the discrete domain geometry is treated as a variable. By simultaneously solving for the flow field and discrete geometry, MDG-ICE is able to produce extremely accurate solutions on very coarse grids as the grid points are automatically repositioned to fit shocks and resolve smooth regions of the flow with sharp gradients. This has significant advantages over traditional shock capturing approaches, such as artificial viscosity and limiting; the former relies on tunable parameters and introduces low-order errors into nominally high-order approximations, whereas the latter

can obstruct iterative convergence and be difficult to apply to high-order solutions on curved elements with arbitrary shapes. Furthermore, since MDG-ICE adapts the grid to satisfy the the weak form, grid interfaces are automatically repositioned to fit a priori unknown shocks with arbitrary topology, thus overcoming key limitations of earlier explicit shock fitting methods. Another form of implicit shock fitting is the high-order implicit shock tracking (HOIST) framework developed by Zahr and Persson [4] and improved in [5, 6], which also treats the discrete geometry as a variable while retaining a standard discontinuous Galerkin method. High-quality solutions to inviscid flows with discontinuities on coarse grids have been achieved using HOIST.

Figure 1 presents representative results for supersonic viscous flow over a half-cylinder at Mach 5 and Reynolds number 10^4. A DG($\mathcal{P}1$) solution (where $\mathcal{P}_p$ denotes the space of polynomials of total degree p on simplicial elements) with artificial viscosity is compared with the MDG-ICE($\mathcal{P}4$) solution without any additional stabilization. The shock in the DG solution is noticeably smeared, and spurious oscillations are visible both at the shock and in the shock layer. On the other hand, the shock profile in the MDG-ICE solution is sharp and free from oscillations. MDG-ICE has also been demonstrated to achieve superior convergence rates and significantly higher accuracy than standard DG in boundary-layer problems.

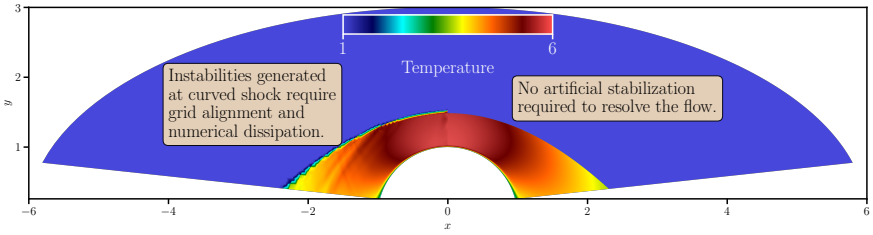

Figure 1: Comparison of the DG($\mathcal{P}1$) (with artificial viscosity) (left) and MDG-ICE($\mathcal{P}4$) (right) solutions to the viscous Mach 5 bow shock at $\mathrm{Re} = 10^4$ [2].

Solution accuracy for approximations of external viscous flows over high-speed vehicles is highly sensitive to both grid alignment and grid resolution at the strong leading shock and within the boundary layer. We equip MDG-ICE with enhanced grid modifications in order to robustly compute high-order solutions on feature adapted grids from an initial coarse grid. In particular, we make use of the mesh-implied metric, which encodes information about the local element size and orientation (even on curved, anisotropic grids) [7]. We incorporate the metric into the Levenberg–Marquardt nonlinear least-squares solver through an anisotropic grid regularization that inhibits grid motion in a manner that is inversely proportional to element lengths as defined by the metric. These tools are combined with the residual, a natural error indicator of least-squares methods, to drive anisotropic mesh refinement. This increases robustness and efficiency and overcomes the generation of "sliver" elements, as illustrated in Figure 2, caused by splitting edges of invalid elements that form as MDG-ICE adapts the grid to resolve the flow. These sliver elements introduce unnecessary degrees of freedom and may be undesirable for parametric studies in which, for example, the angle of attack is varied. Finally, we apply these strategies to accurately compute multidimensional high-speed viscous flows with fewer degrees of freedom and in a more robust manner than in previous work.

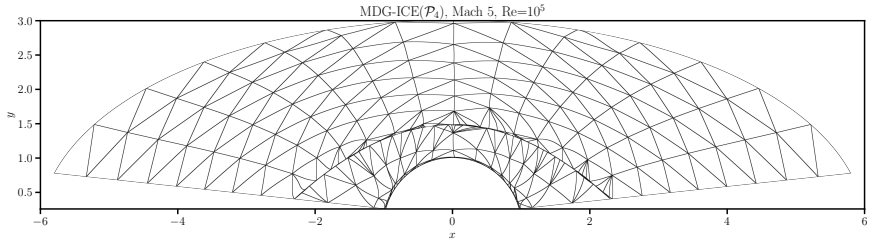

Figure 2: Final mesh for MDG-ICE solution to viscous Mach 5 bow shock at $\mathrm{Re} = 10^5$ [2].

2 Governing equations

Consider the following nonlinear conservation law:

$$\nabla \cdot \mathcal{F}(y, \nabla_x y) = 0 \text{ in } \Omega, \tag{1}$$

where y is the state variable, $\mathcal{F}$ is the flux, $\nabla_x(\cdot)$ denotes the spatial gradient, and Ω is the domain. In the case of a space-time domain of dimension d, the space-time flux is given by

$$\mathcal{F}(y, \nabla_x y) = \left(\mathcal{F}_1^x(y, \nabla_x y), \ldots, \mathcal{F}_{d_x}^x(y, \nabla_x y), y\right), \tag{2}$$

where $d_x = d - 1$ is the number of spatial dimensions and $\mathcal{F}^x(y, \nabla_x y) = \mathcal{F}^c(y) - \mathcal{F}^v(y, \nabla_x y)$ is the spatial flux, consisting of both the convective flux, $\mathcal{F}^c(y)$, and the viscous flux, $\mathcal{F}^v(y)$. The divergence operator in Equation (1) is then the space-time divergence operator, given by

$$\nabla \cdot \mathcal{F}(y, \nabla_x y) = \nabla_x \cdot \mathcal{F}^x(y, \nabla_x y) + \frac{\partial}{\partial t} y. \tag{3}$$

In the case of a spatial domain, the flux is simply the spatial flux and the divergence operator is the spatial divergence operator.

In this study, we consider the viscous Burgers equation and the compressible Navier-Stokes equations.

2.1 One-dimensional viscous Burgers equation

For the one-dimensional viscous Burgers equation, the convective and viscous fluxes are given by

$$\mathcal{F}^c(y) = \left(\frac{1}{2} y^2\right), \quad \mathcal{F}^v(y, \nabla_x y) = \mu \nabla_x y, \tag{4}$$

where μ is the viscosity. The spatial flux is then written as

$$\mathcal{F}^x(y, \nabla_x y) = \left(\frac{1}{2} y^2 - \mu \nabla_x y\right), \tag{5}$$

2.2 Compressible Navier-Stokes equations

The vector of state variables is given by

$$y = \left(\rho, \rho v_1, \ldots, \rho v_{d_x}, \rho E\right), \tag{6}$$

where ρ is the density,$v = (v_1, \ldots, v_{d_x})$ is the velocity vector, and E is the specific total energy. The ith spatial component of the convective flux is

$$\mathcal{F}_i^c(y) = \left(\rho v_i, \rho v_i v_1 + P\delta_{i1}, \ldots, \rho v_i v_{d_x} + p\delta_{i d_x}, \rho H v_i\right), \tag{7}$$

where P is the pressure, δ_{ij} is the Kronecker delta, and $H = (\rho E + p)/\rho$ is the specific total enthalpy. In this work, we assume a calorically perfect gas, such that

$$P = (\gamma - 1)\left(\rho E - \frac{1}{2} \sum_{i=1}^{d_x} \rho v_i v_i\right), \tag{8}$$

where γ is the specific heat ratio, set to 1.4.

The ith spatial component of the viscous flux is

$$\mathcal{F}_i^\nu(y, \nabla_x y) = \left(0, \tau_{1i}, \ldots, \tau_{d_x i}, \sum_{j=1}^{d_x} \tau_{ij} v_j - q_i\right), \tag{9}$$

where q is the heat flux and τ is the viscous stress tensor. The heat flux is expanded as $q = -\kappa \nabla_x T$, where κ is the thermal conductivity and T is the temperature, calculated as $T = P/(\rho R)$, with $R = 287$ denoting the specific gas constant. The ith spatial component of the viscous stress tensor is given by

$$\tau_i = \mu \left(\frac{\partial v_1}{\partial x_i} + \frac{\partial v_i}{\partial x_1} - \delta_{i1} \frac{2}{3} \sum_{j=1}^{d_x} \frac{\partial v_j}{\partial x_j}, \ldots, \frac{\partial v_{d_x}}{\partial x_i} + \frac{\partial v_i}{\partial x_{d_x}} - \delta_{i d_x} \frac{2}{3} \sum_{j=1}^{d_x} \frac{\partial v_j}{\partial x_j} \right), \tag{10}$$

where $\mu : \mathbb{R}^m \to \mathbb{R}_+$ is the dynamic viscosity coefficient given by Sutherland's law. The thermal conductivity is computed using the constant-Prandtl-number assumption, $\mathrm{Pr} = 0.72$.

Two important nondimensional quantities that characterize Navier-Stokes flows are the Reynolds number, Re, and Mach number, Ma, defined as

$$\mathrm{Re} = \frac{\rho |v| L}{\mu}, \tag{11}$$

where L is a characteristic length scale, and

$$\mathrm{M} = \frac{|v|}{c}, \tag{12}$$

where $c = \sqrt{\gamma P/\rho}$ is the speed of sound, respectively.

3 Formulation

3.1 Moving discontinuous Galerkin method with interface condition enforcement

In this subsection, we briefly review the MDG-ICE formulation for compressible viscous flows. Further details can be found in [2].

Let Ω be partitioned by $\mathcal{T}$, which consists of cells κ. Furthermore, we define the set $\mathcal{E}$ of interfaces such that $\bigcup_{\epsilon \in \mathcal{E}} = \bigcup_{\kappa \in \mathcal{T}} \partial\kappa$. The normal over each interface $\epsilon \in \mathcal{E}$ is denoted n. For space-time domains, n_x denotes the spatial normal.

3.1.1 Strong and weak formulations

Consider the following conservation law, constitutive law, and associated interface conditions in strong form:

$$\nabla \cdot \mathcal{F}(y, \sigma) = 0 \text{ in } \kappa \qquad \forall \kappa \in \mathcal{T}, \tag{13}$$

$$\sigma - G(y) \nabla_x y = 0 \text{ in } \kappa \qquad \forall \kappa \in \mathcal{T}, \tag{14}$$

$$[\![n \cdot \mathcal{F}(y, \sigma)]\!] = 0 \text{ on } \epsilon \qquad \forall \epsilon \in \mathcal{E}, \tag{15}$$

$$\{\!\{ G(y) \}\!\} [\![y \otimes n_x]\!] = 0 \text{ on } \epsilon \qquad \forall \epsilon \in \mathcal{E}, \tag{16}$$

where σ is an auxiliary variable, $G(y)$ is the homogeneity tensor that satisfies $G(y)\nabla_x y = \mathcal{F}^v(y, \nabla_x y) = \mathcal{F}^v_{\nabla_x y}(y, \nabla_x y) \nabla_x y$ (assuming the viscous flux is linear with respect to the spatial gradient of the state), and $\{\!\{\cdot\}\!\}$ and $[\![\cdot]\!]$ denote the average and jump operators, respectively. The interface condition (15), which corresponds to the conservation law (13), is known as the jump or Rankine-Hugoniot conditions. The interface condition (16), derived in [2], is associated with the constitutive law (14).

Let the solution spaces Y and Σ be the broken Sobolev spaces

$$Y = \left\{ y \in \left[L^2(\Omega) \right]^m \quad \middle| \forall \kappa \in \mathcal{T}, \quad y|_\kappa \in \left[H^1(\kappa) \right]^m \right\}, \tag{17}$$

$$\Sigma = \left\{ \sigma \in \left[L^2(\Omega) \right]^{m \times d_x} \middle| \forall \kappa \in \mathcal{T}, \nabla_x \cdot \sigma|_\kappa \in \left[L^2(\Omega) \right]^m \right\}. \tag{18}$$

The MDG-ICE weak formulation is then obtained by integrating Equations (13)-(16) against separate test

functions: find $(y,\sigma) \in Y \times \Sigma$ such that

$$\begin{aligned} 0 = & \sum_{\kappa\in\mathcal{T}} \left(\nabla\cdot\mathcal{F}\left(y,\sigma\right) - f, v_y\right)_\kappa \\ & + \sum_{\kappa\in\mathcal{T}} \left(\sigma - G\left(y\right)\nabla_x y, v_\sigma\right)_\kappa \\ & - \sum_{\epsilon\in\mathcal{E}} \left(\left[\!\left[n\cdot\mathcal{F}\left(y,\sigma\right)\right]\!\right], w_y\right)_\epsilon \\ & - \sum_{\epsilon\in\mathcal{E}} \left(\left\{\!\left\{G\left(y\right)\right\}\!\right\}\left[\!\left[y\otimes n_x\right]\!\right], w_\sigma\right)_\epsilon \qquad \forall\left(v_y, v_\sigma, w_y, w_\sigma\right) \in V_y\times V_\sigma\times W_y\times W_\sigma. \end{aligned} \tag{19}$$

where the test spaces are $V_y = \left[L^2\left(\Omega\right)\right]^m$ and $V_\sigma = \left[L^2\left(\Omega\right)\right]^{m\times d}$, with W_y and W_σ defined as the corresponding single-valued trace spaces.

To treat the grid as a variable, the weak formulation (19) is transformed from physical to reference space. Let $u : \hat{\Omega} \to \Omega$ be a continuous, invertible mapping from the reference domain, $\hat{\Omega}$, to the physical domain, Ω. $\hat{\Omega}$ is assumed to be partitioned by $\hat{\mathcal{T}}$, such that $\overline{\hat{\Omega}} = \cup_{\hat{\kappa}\in\hat{\mathcal{T}}}\overline{\hat{\kappa}}$. Furthermore, let $\hat{\mathcal{E}}$ denote the set of interfaces, $\hat{\epsilon}$, such that $\cup_{\hat{\epsilon}\in\hat{\mathcal{E}}}\hat{\epsilon} = \cup_{\hat{\kappa}\in\hat{\mathcal{T}}}\partial\hat{\kappa}$. The solution and test spaces are also now assumed to be defined over reference space. We then define a provisional state operator, $\tilde{e} : Y\times\Sigma\times U \to \left(V_y\times V_\sigma\times W_y\times W_\sigma\right)^*$ for $(y,\sigma,u) \in Y\times\Sigma\times U$, as

$$\begin{aligned} \tilde{e}\left(y,\sigma,u\right) = \left(v_y, v_\sigma, w_y, w_\sigma\right) \mapsto & \sum_{\hat{\kappa}\in\hat{\mathcal{T}}} \left(\left(\mathrm{cof}\left(\nabla u\right)\nabla\right)\cdot\mathcal{F}\left(y,\sigma\right), v_y\right)_{\hat{\kappa}} \\ & + \sum_{\hat{\kappa}\in\hat{\mathcal{T}}} \left(\det\left(\nabla u\right)\sigma - G\left(y\right)\left(\mathrm{cof}\left(\nabla u\right)\nabla\right)_x y, v_\sigma\right)_{\hat{\kappa}} \\ & - \sum_{\hat{\epsilon}\in\hat{\mathcal{E}}} \left(\left[\!\left[s\left(\nabla u\right)\cdot\mathcal{F}\left(y,\sigma\right)\right]\!\right], w_y\right)_{\hat{\epsilon}} \\ & - \sum_{\hat{\epsilon}\in\hat{\mathcal{E}}} \left(\left\{\!\left\{G\left(y\right)\right\}\!\right\}\left[\!\left[y\otimes s\left(\nabla u\right)_x\right]\!\right], w_\sigma\right)_{\hat{\epsilon}}. \end{aligned} \tag{20}$$

The state operator, $e : Y\times\Sigma\times U \to \left(V_y\times V_\sigma\times W_y\times W_\sigma\right)^*$, is defined as

$$e\left(y,\sigma,u\right) = \tilde{e}\left(y,\sigma,b\left(u\right)\right), \tag{21}$$

which imposes geometric boundary conditions via the geometric projection operator, $b(u)$.

The state equation in reference space is $e\left(y,\sigma,u\right) = 0$, such that the corresponding weak formulation in reference space is as follows: find $(y,\sigma,u) \in Y\times\Sigma\times U$ such that

$$\left\langle e\left(y,\sigma,u\right), \left(v_y, v_\sigma, w_y, w_\sigma\right)\right\rangle = 0 \qquad \forall\left(v_y, v_\sigma, w_y, w_\sigma\right) \in V_y\times V_\sigma\times W_y\times W_\sigma. \tag{22}$$

The solution is therefore given by $\left(y,\sigma,b\left(u\right)\right) \in Y\times\Sigma\times U$.

3.1.2 Discretization

To discretize the weak formulation (22), we choose discrete subspaces $Y_h \subset Y$, $\Sigma_h \subset \Sigma$, $U_h \subset U$, $V_{y,h} \subset V_y$, $V_{\sigma,h} \subset V_\sigma$, $W_{y,h} \subset W_y$, and $W_{\sigma,h} \subset W_\sigma$ and define a discrete state operator

$$e_h : Y_h\times\Sigma_h\times U_h \to \mathbb{R}^{\dim\left(V_{y,h}\times V_{\sigma,h}\times W_{y,h}\times W_{\sigma,h}\right)}. \tag{23}$$

For a simplicial grid,

$$Y_h = \left\{ y\in Y \;\middle|\; \forall\hat{\kappa}\in\hat{\mathcal{T}},\, y|_{\hat{\kappa}} \in \left[\mathcal{P}_p\right]^m \right\}, \tag{24}$$

$$\Sigma_h = \left\{ \sigma\in\Sigma \;\middle|\; \forall\hat{\kappa}\in\hat{\mathcal{T}},\, \sigma|_{\hat{\kappa}} \in \left[\mathcal{P}_p\right]^{m\times d_x} \right\}, \tag{25}$$

where $\mathcal{P}_p$ is the space of polynomials spanned by the monomials $\boldsymbol{x}^\beta$ with multi-index $\beta \in \mathbb{N}_0^d$ satisfying $\sum_{i=1}^d \beta_i \leq p$. We set $V_{y,h} = Y_h$ and $V_{\sigma,h} = \Sigma_h$. $W_{y,h}$ and $W_{\sigma,h}$ are selected to be the corresponding single-valued polynomial trace spaces. The discrete subspace U_h of geometric mappings is defined as

$$U_h = \left\{ u \in U \,\middle|\, \forall \hat{\kappa} \in \hat{\mathcal{T}},\, u|_{\hat{\kappa}} \in [\mathcal{P}_p]^d \right\}. \tag{26}$$

3.1.3 Solver

The weak formulation is solved iteratively using unconstrained optimization to minimize $J(y,\sigma,u) = \frac{1}{2}\left\|e_h(y,\sigma,u)\right\|^2$, by seeking a stationary point

$$\nabla J(y,\sigma,u) = e_h'(y,\sigma,u)^* \, e_h(y,\sigma,u) = 0, \tag{27}$$

where $e_h'(y,\sigma,u)^* : \mathbb{R}^{\dim(V_{y,h}\times V_{\sigma,h}\times W_{y,h}\times W_{\sigma,h})} \to Y_h \times \Sigma_h \times U_h$ is the adjoint operator. Given an initialization $(y,\sigma,u)_0$, the solution is repeatedly updated

$$(y,\sigma,u)_{i+1} = (y,\sigma,u)_i + \Delta(y,\sigma,u)_i \qquad i = 0,1,2,\ldots \tag{28}$$

until (27) is satisfied to a given tolerance. We employ a Levenberg-Marquardt method [8, 9] to solve (27), which yields the increment

$$\Delta(y,\sigma,u) = -\left(e_h'(y,\sigma,u)^* \, e_h'(y,\sigma,u) + I_\lambda(y,\sigma,u)\right)^{-1}\left(e_h'(y,\sigma,u)^* \, e_h(y,\sigma,u)\right), \tag{29}$$

where the regularization operator is given by

$$I_\lambda(y,\sigma,u) : (\delta y, \delta\sigma, \delta u) \mapsto (\lambda_y \delta y, \lambda_\sigma \delta\sigma, \lambda_u \delta u), \tag{30}$$

with λ_y, λ_σ, and λ_u denoting the regularization coefficients. We also incorporate a Laplacian-type grid regularization,

$$I_\lambda^\Delta : \delta u \mapsto -\lambda_{\Delta u}\left(b'(u)^* \, \Delta b'(u)\right)\delta u, \tag{31}$$

with $\lambda_{\Delta u} \geq 0$, that introduces a compressibility effect into the grid motion. Further details on the nonlinear solver can be found in [2].

3.2 Anisotropic grid modifications

This subsection introduces the new anisotropic grid modifications that we incorporate into the MDG-ICE formulation to more robustly and efficiently compute viscous flows with high-gradient features.

3.2.1 Anisotropic grid regularization

In previous work [3], following the approach of Zahr et al. [5], the regularization factor $\lambda_{\Delta u}$ was modified to incorporate a factor proportional to the inverse of the element volume. This approach locally stiffens small elements in order to prevent element degeneration, which can inhibit convergence of the nonlinear solver, see also [10]. In this work, we modify the regularization (31) to directly account for element anisotropy as

$$I_\lambda^\Delta : \delta u \mapsto -\lambda_{\Delta u}\left(b'(u)^* \, \Delta \mathcal{H}^{-\alpha} b'(u)\right)\delta u, \tag{32}$$

where $\alpha > 0$ is a parameter and $\mathcal{H}$, in the two-dimensional case, is an element-local, 2×2, symmetric-positive-definite transformation matrix given by [7, 11]

$$\mathcal{H} = \mathcal{M}^{-1/2} = V\Sigma V^T = \begin{bmatrix} | & | \\ \widehat{e}_1 & \widehat{e}_2 \\ | & | \end{bmatrix}\begin{bmatrix} h_1 & 0 \\ 0 & h_2 \end{bmatrix}\begin{bmatrix} — & \widehat{e}_1^T & — \\ — & \widehat{e}_2^T & — \end{bmatrix}. \tag{33}$$

$\mathcal{M}$ is the metric implied by the mesh [7], the columns of V are the (orthonormal) left singular vectors, $\widehat{e}_1$ and $\widehat{e}_2$, of the geometric Jacobian, J, and Σ is a diagonal matrix with the singular values, h_1 and h_2, of J along

the main diagonal. $\mathcal{H}$ projects the unit circle to an ellipse with principal directions $\widehat{e}_1$ and $\widehat{e}_2$ and principal stretching magnitudes h_1 and h_2 [11]. Without loss of generality, we assume that the singular values are ordered such that $h_1 \leq h_2$. $\mathcal{H}^{-\alpha}$ can be expanded as

$$\mathcal{H}^{-\alpha} = V\Sigma^{-\alpha}V^T = \begin{bmatrix} | & | \\ \widehat{e}_1 & \widehat{e}_2 \\ | & | \end{bmatrix} \begin{bmatrix} h_1^{-\alpha} & 0 \\ 0 & h_2^{-\alpha} \end{bmatrix} \begin{bmatrix} — & \widehat{e}_1^T & — \\ — & \widehat{e}_2^T & — \end{bmatrix}. \tag{34}$$

As such, the modified regularization (32) limits grid motion in directions with small element length scales, which is crucial for maintaining grid validity while resolving thin viscous structures. The metric described here is a powerful tool that can be used not only for anisotropic grid regularization, but also for remeshing via a metric-based grid generator [7] in order to maintain high-quality grids, which will be the subject of future work.

3.2.2 Grid refinement

Here, we summarize the framework for adaptively refining the grid as the solver converges and the grid is automatically aligned with thin viscous layers present in the solution. This allows us to start with a relatively coarse grid, which is suitable for an inviscid calculation, and add degrees of freedom as necessary in order to better resolve the thin viscous layers while helping to maintain grid validity. Development of the refinement framework is still ongoing; the final version will be presented in more detail in future work.

One refinement strategy makes use of the residual, a natural error indicator in least-squares-type methods. Specifically, the cell and/or interface residuals are used to flag elements for refinement. Three refinement patterns are currently implemented. In the first, the longest edge of the given cell is refined. In the second, the edge selected for refinement is that which results in the smallest angle between the newly added interface and the interface with the highest face residual. The last refinement pattern is similar to the second, except the face residual normalized by the surface area is considered. The user may specify the maximum number of elements to refine at each adaptation step, in which case the elements with the highest cell/face residuals are selected.

While the above strategy primarily focuses on refining in regions with high residual contributions, other options focus on maintaining element quality. Specifically, we consider the following indicators to flag elements for longest-edge refinement: the minimum value of the determinant of the geometric Jacobian, the minimum length scale according to the mesh-implied metric (i.e., h_1), and the element aspect ratio according to the mesh-implied metric (i.e., h_2/h_1). Other indicators may be considered as well in future work.

4 Results

We apply MDG-ICE, equipped with the anisotropic grid modifications described in Section 3.2, to compute viscous flows with high-gradient features. Unsteady solutions are obtained using a space-time discretization.

4.1 Space-time Burgers viscous shock formation

This section presents results for space-time Burgers viscous shock formation, previously computed using MDG-ICE in [2]. The initial condition is given by

$$y(x, t=0) = \frac{1}{2\pi t_s}\sin(2\pi x) + y_\infty, \tag{35}$$

where x is the spatial coordinate, t is the time, $t_s = 0.5$ is the time of shock formation and $y_\infty = 0.2$ is the freestream velocity. The computational domain is $\Omega = [0,1]\times[0,1]$. Inflow and outflow boundary conditions are applied at the left and right boundaries, respectively. The solution is initialized by extruding the initial condition (35) in the temporal direction.

In [2], in order to obtain a converged solution for $\mu = 10^{-4}$, continuation in μ was necessary. Specifically, a series of problems was solved in which μ was gradually decreased, with the final solution of a given problem used as the initial condition of the subsequent one. Viscosities of $\mu = 10^{-3}$ and $\mu = 5\times10^{-4}$ were considered

before computing the $\mu = 10^{-4}$ case. Here, we aim to obtain converged solutions under the following conditions:

- No continuation in μ
- $\mu = 10^{-5}$, resulting in thinner shocks that are more difficult to resolve
- Space-time triangular elements of quadratic geometric order

We found viscosities of $\mu = 10^{-5}$ to be particularly challenging as the solver tended to approximate the viscous shock corresponding to smaller viscosities as a discontinuity instead of resolving the thin viscous profile. Although we consider this to be a reasonable approximation, it does little to showcase the ability of the improved grid modifications to automatically resolve thin viscous structures. A modification to the generalized constitutive tensor, analogous to the case of a Compressible Navier-Stokes flow as previously detailed [2], would be required in order to resolve these thin viscous structures at smaller viscosities.

In [2], the initial grid consisted of 200 triangular linear elements obtained by splitting each element of a uniform 10×10 quadrilateral mesh into two triangles, resulting in a structured topology. In this study, we consider two more challenging initial grids: (a) a structured grid in which each element of a uniform 5×5 quadrilateral mesh is split into two triangles, and (b) an unstructured 66-element grid. Due to the fewer degrees of freedom and the use of quadratic elements (in terms of geometry), it is significantly more difficult to converge the solution while maintaining a valid grid. As in [2], we compute $\mathcal{P}_5$ solutions.

4.1.1 Structured initial mesh topology

The initial condition and 50-element grid are presented in Figure 3(a). MDG-ICE adjusts the grid geometry to resolve the viscous shock as a sharp yet smooth profile without relying on artificial stabilization. Resolution is dynamically increased near the point of shock formation. The final solution and 140-element grid are given in Figure 3(b). All of the three aforementioned conditions are satisfied. In particular, continuation in μ is not employed. The modified regularization (32) allows for the formation of very high-aspect-ratio but nevertheless valid elements along the viscous shock.

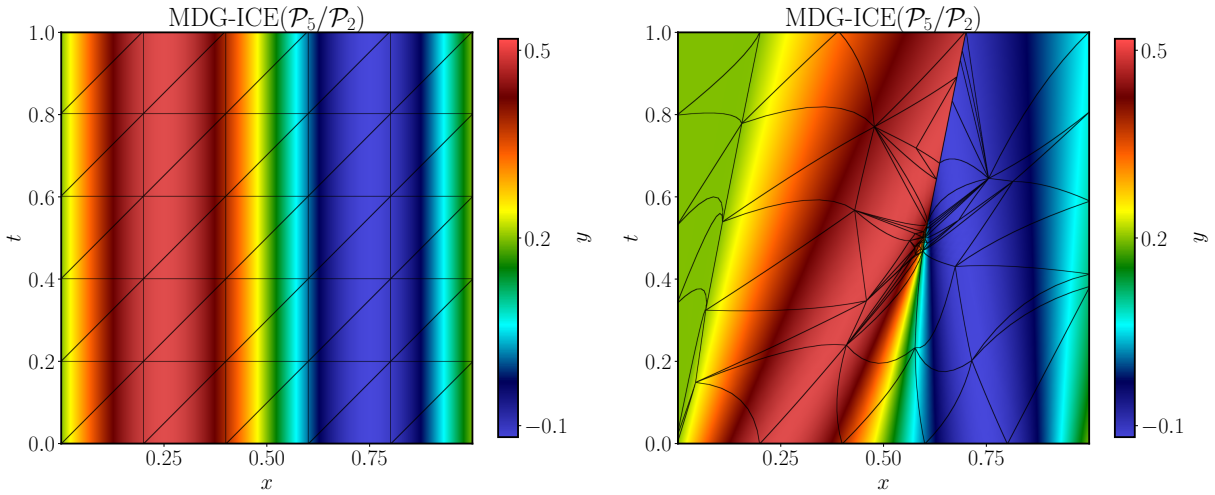

(a) Initial 50-element grid and solution

(b) Final 140-element grid and solution

Figure 3: The space-time Burgers initial and final grid and solution for $\mu = 10^{-5}$ and a structured mesh topology. The initial condition is given in Equation (35).

4.1.2 Unstructured initial mesh topology

Next, we consider a more practical unstructured mesh topology. The initial 66-element grid, along with the initial condition, is displayed in Figure 4(a). Similar to the structured-topology case, the refinement

algorithm increases resolution in the vicinity of the shock. The final solution and 114-element grid are shown in Figure 4(b). Again, continuation in μ is unnecessary.

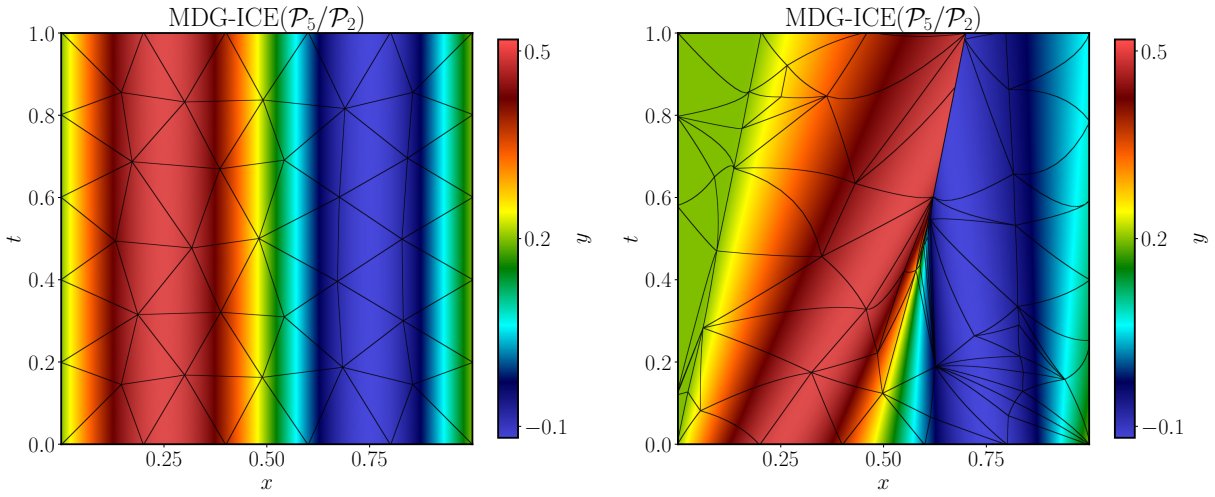

(a) Initial grid and solution

(b) Final 114-element grid and solution

Figure 4: The space-time Burgers initial and final grid and solution for $\mu = 10^{-5}$ and an unstructured mesh topology. The initial condition is given in Equation (35).

4.2 Mach 17.6 viscous bow shock

Next, we compute steady supersonic viscous flow over a circular half-cylinder in two spatial dimensions. The freestream Mach number and Reynolds number (based on the cylinder radius) are 17.6 and 376,930, respectively. Freestream conditions are imposed at the inflow boundary, defined as the ellipse $(x/6)^2 + (y/3)^2 = 1$. Extrapolation is employed at the outflow boundary, and the cylinder boundary, a half-circle of unit radius, is an isothermal no-slip wall with temperature $T_{\text{wall}} = 2.5T_\infty$, where $(\cdot)_\infty$ denotes freestream conditions.

This problem is a common benchmark case for evaluating the ability of numerical techniques to predict hypersonic flows. With simplicial grids, the strong misalignment between the grid and the extremely high gradients in the solution, specifically the strong bow shock and the thin boundary layer, make it notoriously difficult for conventional numerical methods to obtain an accurate surface heat-flux profile. In particular, significant asymmetries were observed using state-of-the-art finite volume techniques [12, 13]; it was only with well-aligned quadrilateral/hexahedral elements that symmetric heating results were obtained. However, the generation of such carefully designed quadrilateral/hexahedral meshes is not always feasible when more complex geometries and/or physics are considered. Note that fairly symmetric heating results have been obtained on simplicial grids with DG schemes equipped with smooth artificial viscosity [14, 15]. In this work, we aim to use the proposed MDG-ICE formulation to achieve symmetric solutions without artificial dissipation.

In previous work, MDG-ICE (without the anisotropic grid modifications described in Section 3.2) was used to compute a simpler version of this problem ($\text{Ma} = 5, \text{Re} = 10^5$) with 768 isoparametric $\mathcal{P}_4$ triangular elements. As in Figure 2, the final grid had a noticeable number of "sliver" elements, resulting in unnecessary (and undesirable) degrees of freedom in the vicinity of the bow shock. Here, with the aforementioned anisotropic grid modifications, we aim to compute this significantly more challenging problem with minimal sliver elements and fewer overall degrees of freedom.

We employ continuation in both the Mach number and the Reynolds number, starting with an MDG-ICE solution corresponding to $\text{Ma} = 5, \text{Re} = 500$. The Mach number is consecutively increased until a Mach 17.6 MDG-ICE solution at $\text{Re} = 500$ is obtained. The 392-element mesh and the temperature, Mach, and pressure fields for this solution are presented in Figure 5. The elements in the vicinity of the shock are anisotropic yet still valid. The MDG-ICE solution is free from oscillations even in the absence of artificial

dissipation.

The Reynolds number is then consecutively increased until the desired value is reached. The final $\mathrm{Ma} = 17.6, \mathrm{Re} = 376,930$ MDG-ICE solution is given in Figure 6. The refinement strategies described in Section 3.2 are employed to increase resolution at the shock and in the boundary layer, resulting in 473 $\mathcal{P}_4$ isoparametric elements. MDG-ICE automatically adjusts the grid geometry in order to resolve said high-gradient features, which become sharper as the Reynolds number is increased. Highly anisotropic elements are observed at the shock and in the boundary layer. The solution is well-resolved and free from spurious artifacts. Compared to previous work, in which 768 elements were required to compute a less challenging $\mathrm{Ma} = 5, \mathrm{Re} = 10^5$ solution, the current grid has significantly fewer elements and is generally free from the aforementioned sliver elements.

Figure 7 presents the surface profiles of pressure coefficient and Stanton number. Both the pressure and heat-flux profiles are highly symmetric. Very slight asymmetry is observed in the latter, likely due to the presence of certain cells with nonpositive Jacobian determinants. Further developments to more robustly prevent the occurrence of cells with nonpositive Jacobian determinants is the subject of ongoing work. Nevertheless, these results represent a considerable improvement over finite volume heating predictions on simplicial grids, highlighting the ability of the proposed MDG-ICE formulation to accurately predict surface quantities without artificial dissipation and/or explicit grid-shock alignment.

5 Conclusions and future work

We introduced anisotropic grid modifications for the moving discontinuous Galerkin method with interface condition enforcement (MDG-ICE). The two main ingredients are as follows:

- Anisotropic regularization in the nonlinear least-squares solver based on the mesh-implied metric
- A dynamic anisotropic mesh refinement framework

These enhancements increase robustness, grid quality, and efficiency in MDG-ICE calculations of high-speed, viscous flows. The proposed MDG-ICE formulation was applied to two test cases involving sharp yet smooth gradients: Burgers viscous shock formation and Mach 17.6 viscous flow over a circular half-cylinder. Well-resolved, oscillation-free solutions were obtained more efficiently and with fewer degrees of freedom than in previous work [2]. We also obtained a highly symmetric shock profile and surface heat-flux profile on a simplicial grid in the cylinder test case, a substantial improvement over state-of-the-art finite volume results. As such, unlike conventional numerical methods, the proposed methodology can resolve very strong bow shocks and thin boundary layers without artificial dissipation and/or explicit grid-shock alignment.

In future work, we will finalize the dynamic refinement framework and incorporate additional mesh modifications to improve grid quality, such as vertex smoothing and edge swaps [10]. Also, since MDG-ICE naturally provides a metric that contains the desired length scales, we plan to leverage metric-based mesh generation/adaptation in order to maintain a high-quality grid. We will then compute more complex viscous hypersonic flows in higher dimensions to further assess the performance of MDG-ICE.

References

[1] A. Corrigan, A.D. Kercher, and D.A. Kessler. A moving discontinuous Galerkin finite element method for flows with interfaces. *International Journal for Numerical Methods in Fluids*, 89(9):362–406, 2019.

[2] A.D. Kercher, A. Corrigan, and D.A. Kessler. The moving discontinuous Galerkin finite element method with interface condition enforcement for compressible viscous flows. *International Journal for Numerical Methods in Fluids*, 93(5):1490–1519, 2021.

[3] A.D. Kercher and A. Corrigan. A least-squares formulation of the moving discontinuous Galerkin finite element method with interface condition enforcement. *Computers & Mathematics with Applications*, 95:143–171, 2021.

[4] M.J. Zahr and P-O Persson. An optimization-based approach for high-order accurate discretization of conservation laws with discontinuous solutions. *Journal of Computational Physics*, 365:105–134, 2018.

[5] M. Zahr, A. Shi, and P.-O. Persson. Implicit shock tracking using an optimization-based high-order discontinuous Galerkin method. *Journal of Computational Physics*, 410:109385, 2020.

[6] Andrew Shi, P-O Persson, and Matthew J Zahr. Implicit shock tracking for unsteady flows by the method of lines. *Journal of Computational Physics*, 454:110906, 2022.

[7] Krzysztof J Fidkowski. *A simplex cut-cell adaptive method for high-order discretizations of the compressible Navier-Stokes equations*. PhD thesis, Massachusetts Institute of Technology, 2007.

[8] K. Levenberg. A method for the solution of certain non-linear problems in least squares. *Quarterly of applied mathematics*, 2(2):164–168, 1944.

[9] D.W. Marquardt. An algorithm for least-squares estimation of nonlinear parameters. *Journal of the society for Industrial and Applied Mathematics*, 11(2):431–441, 1963.

[10] Frédéric Alauzet. A changing-topology moving mesh technique for large displacements. *Engineering with Computers*, 30(2):175–200, 2014.

[11] E.J. Ching and M. Ihme. Efficient projection kernels for discontinuous Galerkin simulations of disperse multiphase flows on arbitrary curved elements. *Journal of Computational Physics*, 435:110266, 2021.

[12] I. Nompelis, T. Drayna, and G. Candler. Development of a hybrid unstructured implicit solver for the simulation of reacting flows over complex geometries. In *34th AIAA Fluid Dynamics Conference and Exhibit*, page 2227, 2004. AIAA-2004-2227.

[13] P. Gnoffo and J. White. Computational aerothermodynamic simulation issues on unstructured grids. In *37th AIAA Thermophysics Conference*, page 2371, 2004. AIAA-2004-2371.

[14] G.E. Barter and D.L. Darmofal. Shock capturing with PDE-based artificial viscosity for DGFEM: Part I. formulation. *Journal of Computational Physics*, 229(5):1810–1827, 2010.

[15] E.J. Ching, Y. Lv, P. Gnoffo, M. Barnhardt, and M. Ihme. Shock capturing for discontinuous Galerkin methods with application to predicting heat transfer in hypersonic flows. *Journal of Computational Physics*, 376:54–75, 2018.

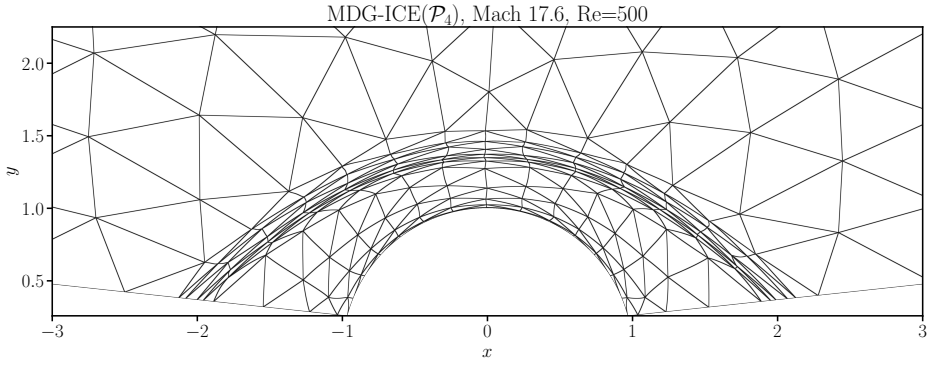

(a) Mesh

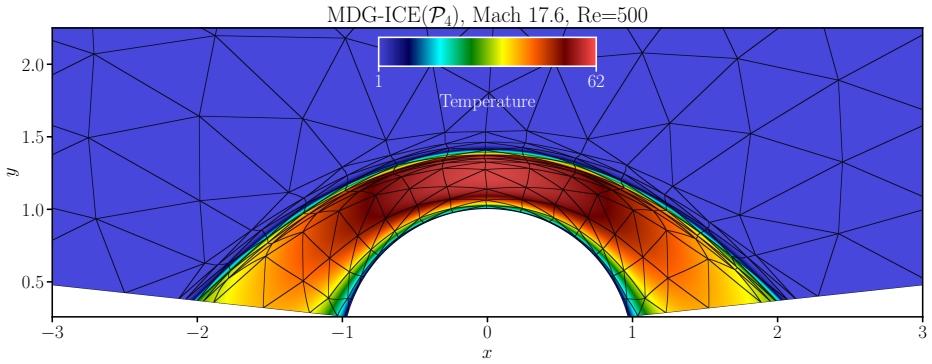

(b) Temperature field

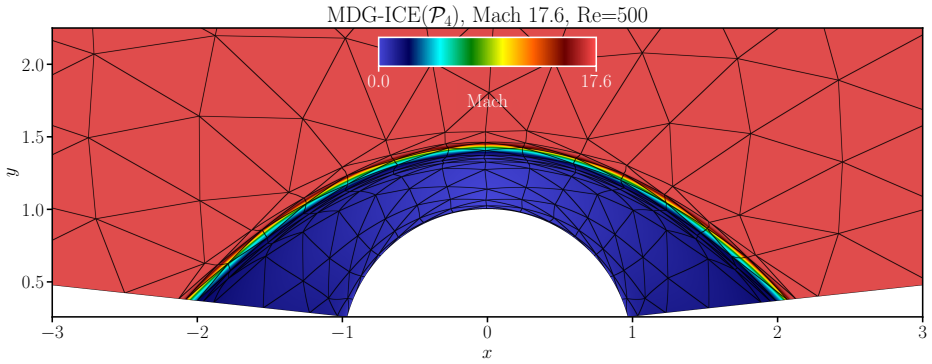

(c) Mach field

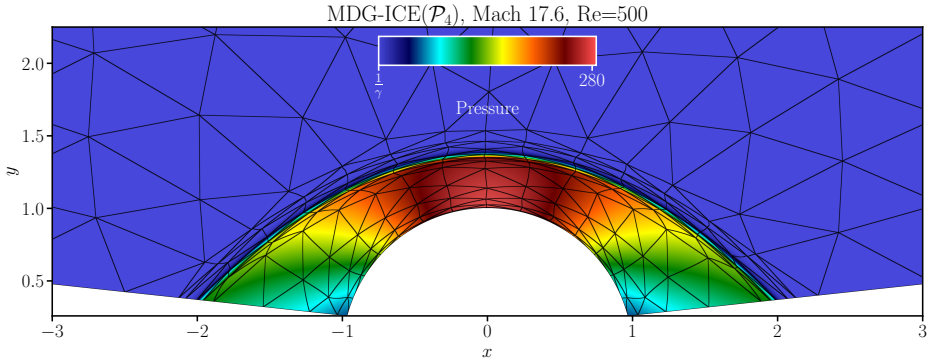

(d) Pressure field

Figure 5: The MDG-ICE solution computed using 392 $\mathcal{P}_4$ isoparametric triangle elements for the viscous Mach 17.6 bow shock at Re = 500.

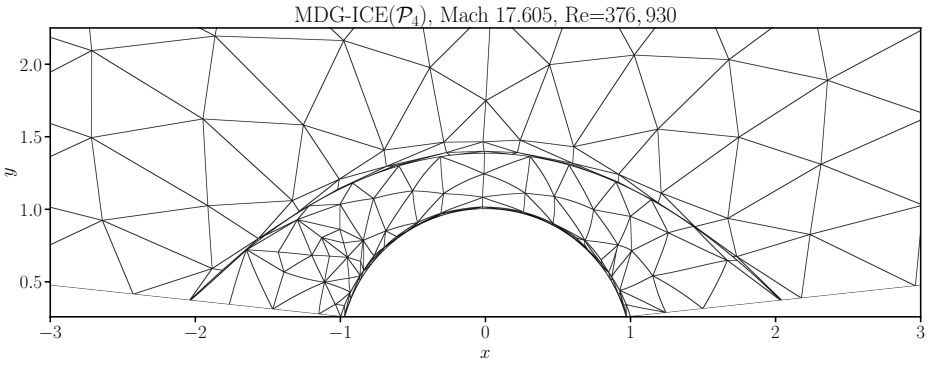

(a) Mesh

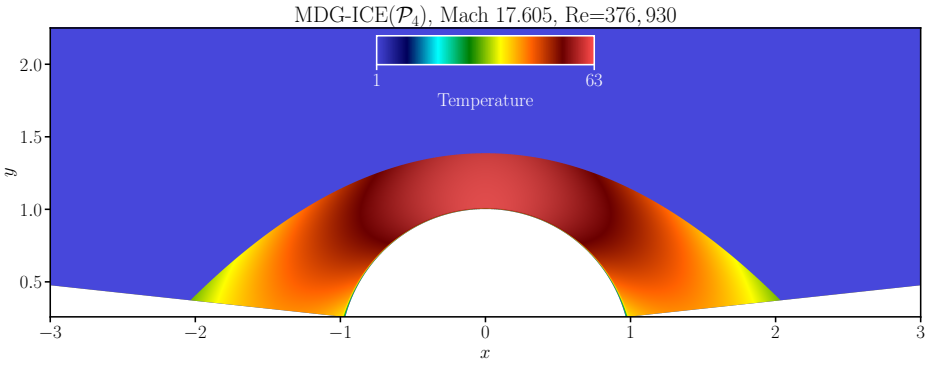

(b) Temperature field

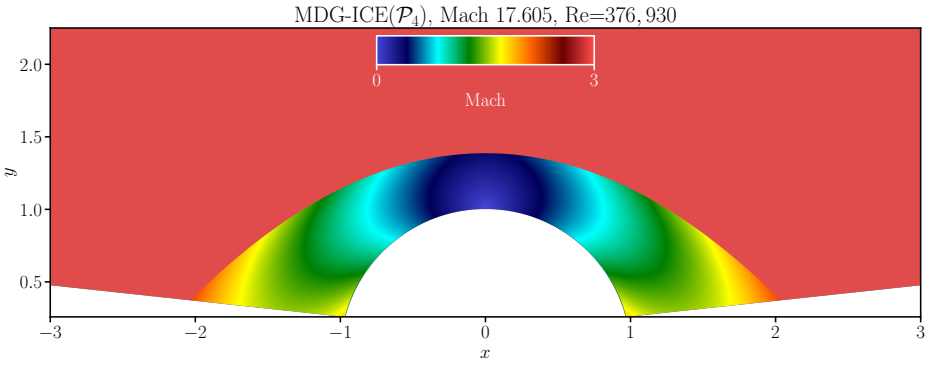

(c) Mach field

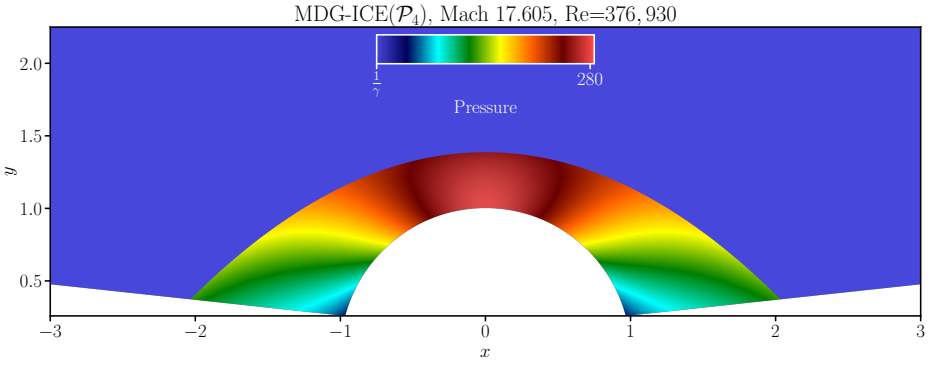

(d) Pressure field

Figure 6: The MDG-ICE solution computed using 473 $\mathcal{P}_4$ isoparametric triangle elements for the viscous Mach 17.6 bow shock at $\mathrm{Re} = 376,930$.

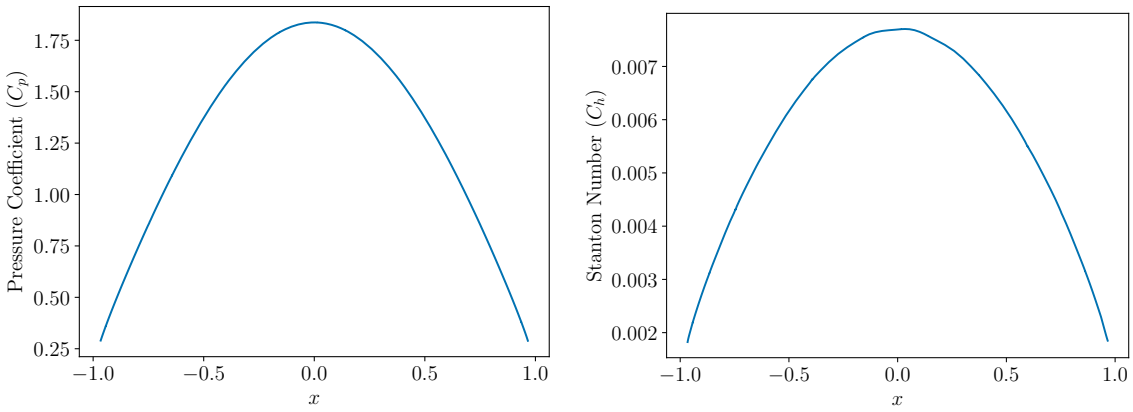

(a) Pressure coefficient profile.

(b) Stanton number profile.

Figure 7: Surface profiles of pressure coefficient and Stanton number for the MDG-ICE solution computed using 473 $\mathcal{P}_4$ isoparametric triangle elements for the viscous Mach 17.6 bow shock at $\mathrm{Re} = 376,930$.